

# Low-cost Quantification of Fluid Flow Parameter Sensitivity using Reduced-order Modeling

Harley Hanes\*

*North Carolina State University, Raleigh, NC 27695*

Michael W. Lee†

*NASA Langley Research Center, Hampton, VA 23681*

Donya Ramezanian‡

*University of Southern California, Los Angeles, CA 90089*

Ralph C. Smith§

*North Carolina State University, Raleigh, NC 27695*

**Sensitivity analysis for computational fluid dynamics (CFD) simulations is a complicated procedure, which still relies, in many cases, on engineering judgment and factors of safety. This is in part because the computational cost of quantifying the simulation's sensitivity to all meaningful parameters (e.g., body surface roughness) and hyperparameters (e.g., subiteration convergence criterion) is intractable for even a single simulation. Reduced-order modeling dramatically lowers this computational cost of simulating fluid flows, but usually only where similar data are already available. In this work, fluid reduced-order models are utilized to quantify flow sensitivity to certain physical parameters for the purposes of improved sensitivity analysis. Characteristic observability and sensitivity are both explored. The sensitivity results enable more informed CFD frameworks and more rigorous uncertainty bounds on the resulting data.**

## I. Nomenclature

$a$	= proper orthogonal decomposition coefficient
$b$	= boundary penalty term
$B$	= boundary penalty term integrated matrix
$C$	= reduced-order model constant vector
$d$	= Morris screening function sensitivity
$E_k$	= integrated kinetic energy
$\ell$	= relative length of the maximum function axis
$L$	= reduced-order model linear matrix
$M$	= reduced-order model mass matrix
$P$	= fluid static pressure
$Q$	= reduced-order model nonlinear matrix
$\mathbb{R}$	= the real number space
$Re$	= Reynolds number
$S$	= physical system dimension
$t$	= time
$u$	= fluid velocity vector
$\bar{v}$	= velocity magnitude
$V$	= integrated vorticity

\*Doctoral Candidate, Department of Mathematics, North Carolina State University.

†Research Aerospace Engineer, Configuration Aerodynamics Branch, NASA Langley Research Center, AIAA Member.

‡Postdoctoral Scholar, Viterbi School of Engineering, University of Southern California.

§Distinguished University Professor, Department of Mathematics, North Carolina State University.

$W$	= quadrature weights
$\mathbf{x}$	= position vector of dimension $S$
$\alpha$	= lid cavity velocity boundary coefficient
$\Delta$	= parametric step size
$\Gamma$	= fluid domain boundary
$\theta$	= parameter sample
$\phi$	= proper orthogonal decomposition mode
$\Phi$	= complete modal matrix
$\mu$	= Morris sensitivity mean
$\mu^*$	= Morris sensitivity absolute mean
$\sigma$	= Morris sensitivity standard deviation
$\kappa$	= boundary penalty strength
$\xi$	= mean-reduction basis function location
$\Upsilon$	= boundary penalty restriction term
$\omega$	= vorticity
$\Omega$	= fluid domain
BP-POD-ROM	= Boundary-Penalized POD-based ROM
CFD	= Computational Fluid Dynamics
EDL	= Entry, Descent and Landing
MLUQ	= Machine Learning with Embedded Uncertainty Quantification
POD	= Proper Orthogonal Decomposition
ROM	= Reduced-order Model

## II. Background and Motivation

PLANETARY entry, descent, and landing (EDL) is a necessary and challenging component of many space missions. To survive the extreme aerodynamic environments induced in these mission stages, as well as touch down within as small a landing ellipse as possible, vehicles must be designed with rigorous tolerances and operate within a carefully limited trajectory window. As future landers and their atmospheric trajectories depart further from existing, flight-tested missions, high-fidelity preflight uncertainty quantification and sensitivity analysis becomes increasingly necessary for mission success. This is one aspect of the Mars Lander Aerodynamic Model Data Fusion using Machine Learning with Embedded Uncertainty Quantification (AeroFusion-MLUQ) initiative recently conducted by the NASA Langley Research Center and collaborating universities [1].

Sensitivity analysis quantifies how variability in model outputs, such as velocity or drag coefficients, is apportioned to variability of explicitly included model parameters such as Reynolds number. Sensitivity analysis has established use for quantifying the influence of atmosphere conditions and initial trajectory uncertainty on EDL trajectories [2–4]. Parameters with high sensitivity may require more accurate measurement or can be adjusted to improve performance whereas parameters with low sensitivity may be fixed for model reduction [5]. An important classification of sensitivity analysis methods are whether they are local – measuring sensitivity at a single set of parameter values – or global – quantifying sensitivity over an assumed distribution of parameter values. Local methods are more computationally efficient but cannot quantify dependencies over the admissible parameter space [5]. In this work, we implement a global method, termed Morris screening, and assess its strengths and weaknesses in the EDL context [6]. Morris screening globally averages local sensitivities to permit quantification of sensitivity across parameter distributions without the high computational costs of other global methods such as Sobol analysis [7].

Sensitivity analysis methods typically require hundreds to tens of thousands of model evaluations, making them intractable for implementation on even medium-fidelity conventional computational models. However, lower-cost reduced-order models (ROMs) enable fast enough data throughput to enable accurate sensitivity analysis. A common method is proper orthogonal decomposition (POD)-based Galerkin reduced-order modeling (POD-ROM), which transforms the fluid dynamics problem into an efficiently spanned mode space and reduces the governing equations to a system of temporal ordinary differential equations. However, with a few exceptions, most design-relevant parameters are not explicitly expressed in POD-ROMs, which limits their use for sensitivity analysis.

In this work, we introduce a boundary penalty method to a standard POD-ROM. Boundary penalties have an established use in incompressible POD-ROMs quantifying boundary information to improving stability [8, 9]. Boundary penalties also enable more explicit control of the ROM-simulated boundary conditions, thereby increasing the number

of parameters that can be assessed within the sensitivity analysis. Within conventional wind tunnel- and CFD-centric design cycles, the significance of unavoidable differences in both far- and near-field boundary conditions are often difficult to study directly. This framework addresses that limitation. Gust responses [10] and vehicle surface roughness [11] are just two types of parametric and hyperparametric sensitivities, which can be quantified using such a boundary penalty method within the POD-ROM.

We test this methodology using boundary penalties to compute POD-ROM sensitivity to boundary conditions on an incompressible lid-driven cavity. We measure sensitivity of vorticity and kinetic energy when varying boundary conditions between regularized and unregularized. To the authors' knowledge, this is the first study of an incompressible lid-driven cavity flow's sensitivity to boundary condition transition from regularized to unregularized. Studies investigating intermediate boundary conditions in viscoelastic lid-driven cavities exist, but we do not derive expected results from this study due to the large differences in flow characteristics between turbulent incompressible flows and low-Reynolds number viscous flows [12]. Therefore, we compare studies of streamline characteristics of regularized and unregularized lid-driven cavities at different Reynolds numbers [13, 14].

We present a discussion of Morris screening sensitivity analysis in Section III.A and derive the incompressible formulation of the proper orthogonal decomposition-based reduced-order model with boundary penalty, BP-POD-ROM, in Section III.B. We then provide a brief description of a 2-D regularized lid-driven cavity model selected to test the method in Section III.C. Finally, we present Morris screening results on the test case, exploring the sensitivity of physical parameters including Reynolds number and boundary condition compared to model parameters of penalty strength and the mean decomposition in Section IV. We intend as future work extension of our method to compute sensitivity of compressible Navier-Stokes flows around an Orion lander to lander surface roughness nondimensional quantities such as Reynolds number.

### III. Methodology

#### A. Morris Screening

To compute the sensitivity of a BP-POD-ROM to model parameters, we utilize Morris screening. Morris screening is a one-at-a-time (OAT) quasiglobal sensitivity analysis method, which approximates the local derivatives at parameter values drawn from an assumed distribution [6]. Morris screening can be used to approximate derivative-based sensitivity measures (DGSM), which define sensitivity to be the partial derivative of model outputs to model inputs, integrated over parameter distributions [5, 15]. The primary sensitivity indices that Morris screening calculates are the mean  $\mu_i$ , absolute mean  $\mu_i^*$ , and standard deviation  $\sigma_i$ . Formulae for these indices are,

$$d_i^j = \frac{f(\xi, \theta^j + \Delta e_i) - f(\xi, \theta^j)}{\Delta}, \quad \mu_i = \frac{1}{N} \sum_{j=1}^N d_i^j, \quad \mu_i^* = \frac{1}{N} \sum_{j=1}^N |d_i^j|, \quad \sigma_i = \sqrt{\frac{1}{N-1} \sum_{j=1}^N (d_i^j - \mu_i)^2}, \quad (1)$$

for a parameter  $i$  with  $N$  parameter samples, a step-size of  $\Delta$ , where  $e_i$  is the unit vector for parameter  $i$ . Selection of  $\Delta$  determines how finely the parameter space is searched around each parameter sample  $\theta^j$ . Very small values provide a finite-difference derivative approximation whereas large values instead quantify large-scale function variations [5]. We normalize all parameter ranges to  $[0, 1]$  before implementing Morris screening for nondimensional scaling of  $\Delta$ , assume parameters are uniformly distributed to  $[0, 1]$ , and use  $\Delta = 10^{-4}$ . We sample parameters with quasirandom Sobol samples, which increases accuracy of Morris screening compared to random sampling [16].

The absolute mean  $\mu_i^*$  quantifies the sensitivity magnitude where parameters with larger  $\mu_i^*$  have greater sensitivity over the sampling region. It provides a similar measurement as total variance from Sobol analysis, which quantifies how variance in outputs is apportioned to variance in inputs, but is more computationally expensive, more impacted by error in assumed parameter distributions, and assumes parameters are independently distributed [5]. The absolute mean is generally used, instead of the mean sensitivity, since sensitive parameters can have  $\mu_i \approx 0$  due to cancellation of opposite signs in partial derivatives. Morris screening's  $\sigma_i$  measures the standard deviation of the sensitivity and identifies parameters that may have nonlinear or coupled effects on a quantity [7]. Additionally, parameters with large  $\sigma_i$  compared to  $\mu_i^*$  may be highly sensitive for only a small portion of their distribution.

#### B. POD-ROM with Boundary Penalty

We derive a proper orthogonal decomposition-based reduced order model with boundary penalty, BP-POD-ROM, by introducing a penalty term enforcing the boundary condition into a standard reduced order model. Boundary-penalties

have a well established use in POD-ROMs improving stability of solutions [8, 17]. We mirror the POD-ROM derivation outlined in Ref. [18], using the penalty formulation found in Ref. [8]. We also extend the method in Ref. [18] for using matrix algebra to compute POD-ROM terms  $B$  and  $B^0$  corresponding the boundary penalty. We begin with an incompressible Navier-Stokes system in  $S$  dimensions with Dirichlet boundary conditions,

$$\begin{cases} \partial_t u^i + u^j \nabla^j u^i = -\nabla^i P + \frac{1}{Re} \nabla^2 u^i & x \in \Omega \subset \mathbb{R}^S \\ u = u_\Gamma & x \in \Gamma = \partial\Omega \end{cases}, \quad (2)$$

where  $u^i(\mathbf{x}, t)$  is the velocity in the  $i^{th}$  direction and  $P$  is the pressure. We note that POD-ROM solutions can deviate from the boundary conditions since explicit enforcement of the boundary is lost in POD formulation [8]. Therefore, to enforce the boundary condition  $\Gamma$  when the modal basis deviates, we define the boundary penalty term

$$b_\Gamma^i(\mathbf{x}, t; \kappa) = \kappa \Upsilon(\mathbf{x}) (u^i - u_\Gamma^i), \quad (3)$$

where  $\Upsilon$  restricts the term to the boundary such that,

$$\Upsilon(\mathbf{x}) = \begin{cases} 1 & \mathbf{x} \in \Gamma \\ 0 & \mathbf{x} \notin \Gamma \end{cases}. \quad (4)$$

Here  $\kappa > 0$  determines the the strength of the penalty [8]. We then add the penalty to the Navier-Stokes equations and construct the penalized system

$$\partial_t u^i + u^j \nabla^j u^i + b_\Gamma^i(\mathbf{x}, t; \kappa) = -\nabla^i P + \frac{1}{Re} \nabla^2 u^i. \quad (5)$$

To compute the POD-ROM of the penalized system, we decompose the velocity by assuming  $u^i = u_0^i + u_d^i$ , where  $u_0^i(\mathbf{x})$  is a smooth time-constant velocity field that quantifies boundary conditions, in the case of the lid-driven cavity, this is the temporal mean of the flowfield, and  $u_d^i(\mathbf{x}, t)$  is the remaining portions of the flow with homogeneous Dirichlet boundary conditions. By separating  $u^i$  into its two subcomponents, we expand Equation 2 into

$$\partial_t u_d^i = -u_0^j \nabla^j u_0^i - u_0^j \nabla^j u_d^i - u_d^j \nabla^j u_0^i - u_d^j \nabla^j u_d^i - \nabla^i P + \frac{1}{Re} (\nabla^2 u_0^i + \nabla^2 u_d^i) - \kappa \Upsilon(\mathbf{x}) (u_0^i - u_\infty^i + u_d^i). \quad (6)$$

We then expand  $u_d^i$  into a linear modal sum, which separates the spatial and the temporal velocity components:

$$u_d^i(\mathbf{x}, t) = a_n(t) \phi_n^i(\mathbf{x}). \quad (7)$$

Using the modal decomposition, we can expand Equation 6 into  $T$  (the number of flow snapshots) differential equations for modal coefficients given by the following equation.

$$\phi_n^i \partial_t a_n = -a_n a_m \phi_n^j \nabla^j \phi_m^i - \nabla^i P - (u_0^j \nabla^j \phi_n^i + \phi_n^j \nabla^j u_0^i - \frac{1}{Re} \nabla^2 \phi_n^i) a_n - u_0^j \nabla^j u_0^i + \frac{1}{Re} \nabla^2 u_0^i - \kappa (a_n \phi_n^i + u_0^i - u_\infty^i) |_\Gamma \quad (8)$$

Multiplying this equation by the modal basis  $\{\phi\}$  and integrating yields the Galerkin weak form for Navier-Stokes. The resulting temporal differential equations for  $a_n(t)$  can be expressed by the system

$$[M] (\dot{a}) = (a)^T [Q] (a) + \left( [L^0] + \frac{1}{Re} [L^{Re}] + \kappa [B] \right) (a) + (P) + (C^0) + \frac{1}{Re} (C^{Re}) + \kappa [B^0]. \quad (9)$$

Here formulae for  $M$ ,  $Q$ ,  $L^0$ ,  $L^{Re}$ ,  $C^0$ , and  $C^{Re}$  can be found in Ref. [18], and

$$B_{kn} = -(\phi_k^i, \phi_n^i)_{L^2(\Gamma_1)} = - \int_{\Gamma} \phi_k^x \phi_n^x + \phi_k^y \phi_n^y dS, \quad (10)$$

$$B_{kn}^0 = (\phi_k^i, u_\infty^i - u_0^i)_{L^2(\Gamma)} = \int_{\Gamma_1} \phi_k^x (u_\infty^x - u_0^x) + \phi_k^y (u_\infty^y - u_0^y) dS. \quad (11)$$

To calculate  $B$  and  $B^0$  in two dimensions with  $T$  flow samples and  $S$  spatial points, we first assume prior derivation of POD modal matrix  $\Phi$  [17] and boundary quadrature weights  $W$ . With these computed, the indices of  $B$  and  $B^0$  are given by,

$$B_{kn} = \sum_{(x,y) \in Z} \sum_{i=1}^S \Phi_{xyk}^i \Phi_{xyn}^i W_{xy}, \quad (12)$$

$$B_k^0 = \sum_{(x,y) \in Z} \sum_{i=1}^S \Phi_{xyk}^i (u_{\Gamma,xy}^i - u_{0,xy}^i) W_{xy}, \quad (13)$$

where  $Z$  is the subset of points in the discretization of  $\Omega$  lying on  $\Gamma$ . We also note that  $P \equiv 0$  in incompressible POD-ROMs due to the divergence-free characteristic of POD modes, but that this property is not guaranteed with the addition of the boundary penalty terms [8].

We can compute  $B$  and  $B^0$  using the matrix systems

$$B = \left[ \Phi[z, :]^T \circ \begin{pmatrix} W[z] \\ W[z] \end{pmatrix} \right] \cdot \Phi[z, :] \quad (14)$$

$$B^0 = \left[ \Phi[z, :]^T \circ \begin{pmatrix} W[z] \\ W[z] \end{pmatrix} \right] \cdot (u_{\infty} - u_0[z]), \quad (15)$$

where  $\circ$  denotes the Hamarand product.

### C. Lid-Driven Cavity Test Case

To test the implementation of the BP-POD-ROM, we utilize the incompressible 2-D regularized lid-driven cavity. This flow regime has been studied exhaustively, including significant research on behaviors at different Reynolds numbers and boundary conditions [19]. Lid-driven cavity problems are classified as regularized or unregularized according to their boundary condition. All 2-D lid-driven cavities are rectangular domains with homogeneous Dirichlet boundary conditions on three walls with a nonhomogeneous Dirichlet boundary condition parallel to the fourth wall. In the unregularized case, the nonhomogeneous condition is constant along the boundary, causing a discontinuity at the corners. In the regularized case it is a smooth nonnegative definite function that converges to zero at both boundary edges, eliminating the discontinuity [20]. Both cases have similar dynamics and bifurcations but the unregularized lid-driven cavity experiences them at lower Reynolds numbers [13, 19].

For snapshot data, we use regularized lid-driven cavity simulations computed via direct numerical simulations (DNS) at  $Re = 17,000$  and  $Re = 25,000$  and at a discretization of  $256 \times 256$  points [13, 21]. At the lower of these two Reynolds numbers, the flow exhibits quasiperiodic dynamics; at the higher Reynolds number, the flow is fully aperiodic and formally chaotic. We form a snapshot matrix using the first 150 time-steps and reduce them to 100 POD modes, which contain 99.99% of the snapshot matrix mean fluctuating kinetic energy. We define the boundary condition

$$u_{\Gamma}(x; \alpha) = |(1-x)(1+x)|^{2\alpha}. \quad (16)$$

We note that  $u_{\Gamma}(x, 1)$  is equivalent to the regularized boundary,  $u_{\Gamma}(x, 0)$  is equivalent to the unregularized boundary, and  $u_{\Gamma}(x; \alpha)$  is well-defined for  $x \in [0, 1]$  so the boundary condition is suitable for continuous perturbation of  $\alpha$  in Morris screening.

For the flow reduction snapshot  $u_0^i$ , we used an artificial snapshot computed from a stream function created by summing weighted Gaussian functions

$$f_i(x; \xi, \ell, \theta) = e^{-(x-\xi)^T \Sigma (x-\xi)}, \quad \Sigma = 20 \begin{bmatrix} \ell \sin(\theta) & -\ell \cos(\theta) \\ \cos(\theta) & \sin(\theta) \end{bmatrix}, \quad (17)$$

where  $\xi \in [-1, 1]^2$  is the location of the peak of the function,  $\ell > 0$  is the relative length of the primary axis of the function, and  $\theta \in (0, \pi)$  is the orientation of the primary axis. Once the velocity is computed from a stream function, we normalize it so the maximum velocity magnitude is equal to parameter  $\bar{v} \in (0, 1)$ . Figure 1 shows the vorticity of the mean-reduction at base parameter values with the center of each basis function labeled. Functions 1-3 correspond to the

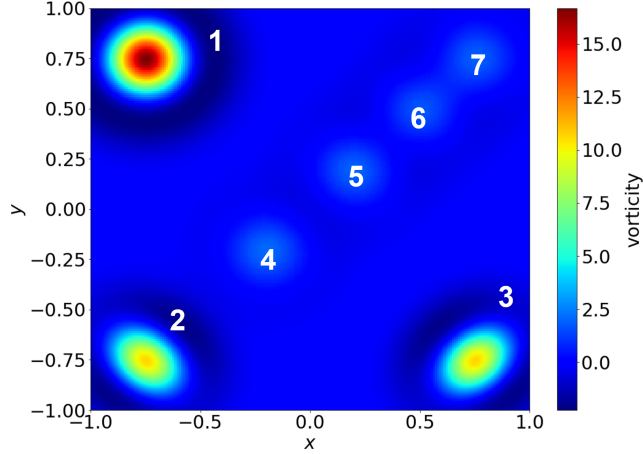


**Fig. 1** Vorticity of artificial mean-reduction using Gaussian basis functions. Functions 1-3 correspond to areas of high vorticity, 4-5 to low velocity regions, and 6-7 to the main rotational flow.

high vorticity eddies, functions 4-5 correspond to the low-velocity region of the flow, and functions 6-7 correspond to the main rotational flow. This adjustment was performed for the purpose of additional sensitivity analyses detailed in subsequent discussion.

To test the BP-POD-ROM, we examine the sensitivity of 1) global kinetic energy, 2) global vorticity, and 3) local vorticities to a) Reynolds number, b) the boundary coefficient  $\alpha$ , c) the penalty strength  $\kappa$ , and d) the mean-reduction defined by the location  $\xi$ , relative axis length  $\ell$ , orientation  $\theta$ , and maximum velocity  $\bar{v}$ , of each basis function in the mean-reduction. Comparing flow characteristics of regularized and unregularized lid-driven cavities, we observe that unregularized lid-driven cavities experience vorticity closer the boundary corner behind the driving lid, top-left corner with our orientation, likely due to the higher boundary velocity in the area causing more flow into and then out of the corner [13, 14]. Therefore, we anticipate the vorticity behind the driving lid to exhibit higher sensitivity to the boundary condition and penalty,  $\alpha$  and  $\kappa$ , than other locations in the domain. Additionally, we expect the method to be insensitive to mean-reduction perturbation in other areas of the domain that exhibit fewer differences between regularized and unregularized boundary conditions.

For Morris screening, parameters are sampled uniformly. To quantify a range of bifurcations, we sample Reynolds number within [11,000, 20,000] for the  $Re = 17,000$  dataset and [19,000, 28,000] for the  $Re = 25,000$  dataset to check stability over large Reynolds number perturbations. Whereas both of these ranges include both quasiperiodic and aperiodic flow, the lower range is primarily quasiperiodic and the higher range is primarily aperiodic. We sample  $\log_{10}(\alpha)$  and  $\log_{10}(\kappa)$  instead of  $\alpha$  and  $\kappa$  since both parameters' effects are identifiable on an exponential scale [8]. We sample  $\log_{10}(\kappa)$  between [-12, 2] to include the effect of having no boundary penalty and we sample  $\log_{10}(\alpha)$  within [-2, 0] since at  $\alpha = 0.01$  and our discretization, the boundary velocity at the points closest to the corners is 0.99 making it nearly unregularized. We sample  $\bar{v}$ , and  $\ell$  for each function within  $\pm 25\%$  of their base values and sample  $\theta$  within  $[0, 2\pi]$  for each function. We sample the  $x$  and  $y$  coordinates of each basis within 0.2 nondimensional spatial units of their base values. The full list of parameters with assumed base values and sampling ranges is provided in Appendix A. Note that the base values are not used in the computation of Morris indices.

To quantify the effect of parameter variations globally, we compute the kinetic energy,  $K_E$ , and the integrated vorticity  $V$ . We also measure the local effects of parameter variations using seven local vorticities,

$$V_i = \int_{B_i} \omega(x) dx, \quad B_i = \{x \in [-1, 1]^2 \mid \|x - \xi_i\| \leq 0.2\}, \quad (18)$$

where  $\xi_i$  is the base location for the  $i^{th}$  mean-reduction function. The local vorticities allow differentiating parameter effects at characteristic locations of the flow and whether the effects of local perturbations to the mean-reduction are limited to that region. We measure sensitivities at  $t = 150$ , the final snapshot in the data, and at  $t = 300$  to observe if any changes in sensitivities occur when solving the BP-POD-ROM for snapshots not provided by data.

#### IV. Results and Discussion

Figure 2 shows Morris absolute mean sensitivities for locally integrated vorticities with respect to Reynolds number, the boundary condition exponent, penalty strength, and mean-reduction characteristics at  $Re = 17,000$  and  $Re = 25,000$ . At both Reynolds numbers, the local vorticities, except for the high vorticity eddies  $V_1$ ,  $V_2$ , and  $V_3$ , are insensitive to all parameters. We note that the vorticity in the bottom-left is significantly more sensitive to the boundary condition and penalty strength than the vorticity in the top-left is, even though that is the region adjacent to the perturbed boundary. Additionally, the sensitivity of the third vorticity region, corresponding to the bottom-right, is significantly more sensitive at  $Re = 25,000$  than at  $Re = 17,000$ . This may be due to the increased complexity of the shear layer and counterrotating corner vortex at the higher Reynolds number. To further investigate differences in locally integrated vorticities, we show in Figure 3 the sensitivity of the  $x$ -velocity at each cell to the boundary condition. As anticipated, both Reynolds number cases have high sensitivities along the edge of the rotational flow, with highest sensitivity in the high-vorticity areas near the corners. However, we note that the sensitivity at the top corners is minimal, even though this is the region of greatest difference between regularized and unregularized lid-driven cavity boundary conditions. Low-sensitivity in this region highlights a limitation of POD-ROMs that they cannot quantify dynamics not present in the initial POD basis and these regions are relatively stagnant in the unregularized POD basis. However, the boundary penalty still exhibits expected sensitivity in high-vorticity corners and at the edge of the rotational flow while having minimal sensitivity in other regions despite mean-reduction perturbation.

Figures 4 and 5 show the Morris screening absolute mean and standard deviation of sensitivity at  $t = 150$  proportional to the maximum sensitivity for each quantity. We restrict these plots to the sensitive parameters identified in Figure 2 and divide by the maximum sensitivity for each quantity to identify which parameter is most sensitive for each quantity. We observe that  $\bar{v}_1$  is the most sensitive parameter for both  $Re = 17,000$  and  $Re = 25,000$ , and that all quantities are insensitive to all other mean decomposition parameters. For  $Re = 17,000$ , Reynolds number is the next most sensitive parameter and the penalty strength and boundary condition are relatively insensitive, whereas for  $Re = 25,000$ , all three parameters have similar sensitivities for all quantities. We observe that the mean-reduction parameters, excepting  $\bar{v}_1$ , all have low standard deviations, indicating that sensitivity of these parameters is small for all parameter combinations sampled. Additionally, we note that  $\bar{v}_1$  has the highest standard deviation of sensitivity for most quantities, suggesting that kinetic energy and vorticity may be insensitive to  $\bar{v}_1$  at some parameter combinations, even though  $\bar{v}_1$  is the most sensitive parameter. For both  $Re = 17,000$  and  $Re = 25,000$ ,  $\bar{v}_1$  had the largest  $\mu^*$  for all quantities, but  $\kappa$  or  $\alpha$  have higher  $\sigma^*$  for the kinetic energy, and the locally integrated vorticities for the high-vorticity regions.

Figure 6 shows the Morris screening absolute mean sensitivity at  $t = 300$  proportional to the maximum sensitivity for each quantity. We note that for both Reynolds numbers, the relative sensitivity of the mean decomposition increases significantly compared to  $t = 150$ . However, all quantities remain more sensitive to  $Re$ ,  $\alpha$ ,  $\kappa$ , and  $\bar{v}_1$  than the other mean decomposition parameters. For  $Re = 17,000$ , we observe increases to the relative sensitivity of all quantities to most mean-reduction parameters. However, all quantities remain less sensitive to mean-reduction parameters, with the exception of  $\bar{v}_1$ , than to  $Re$ ,  $\alpha$ , and  $\kappa$ . We observe similar increases to sensitivity for  $Re = 25,000$  but with greater increases to sensitivity of local vorticities to mean-reduction parameters in the corners of the lid-driven cavity. We also note that for both Reynolds numbers, the relative sensitivity of all quantities  $Re$  increases but  $\bar{v}_1$  is still the most sensitive parameter.

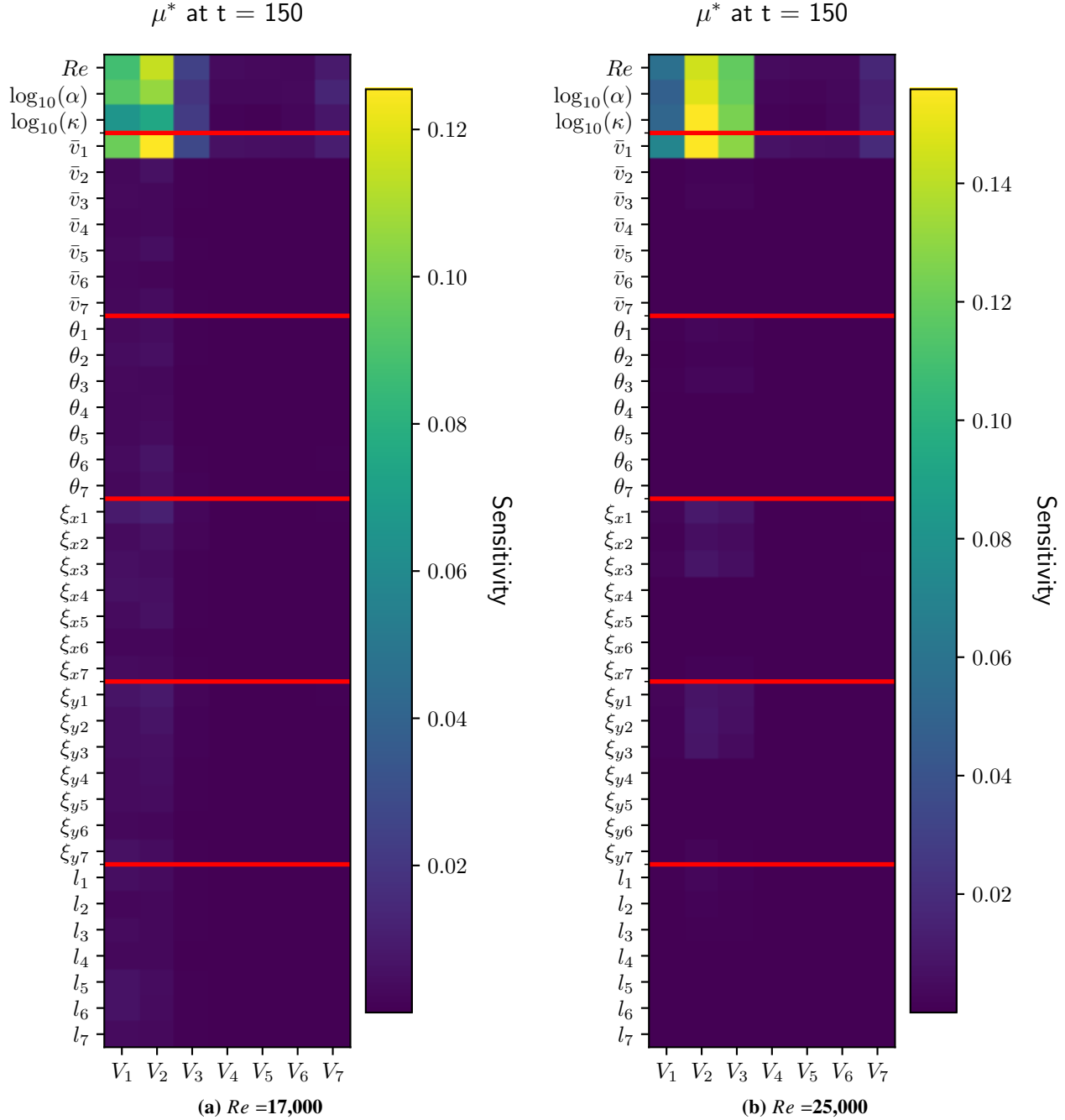


**Fig. 2** Morris mean absolute sensitivity results for local integrated vorticities at  $t = 150$  and at (a)  $Re = 17,000$  and (b)  $Re = 25,000$ . Each cell is  $\mu^*$  for the corresponding quantity (x-axis) and parameter (y-axis).

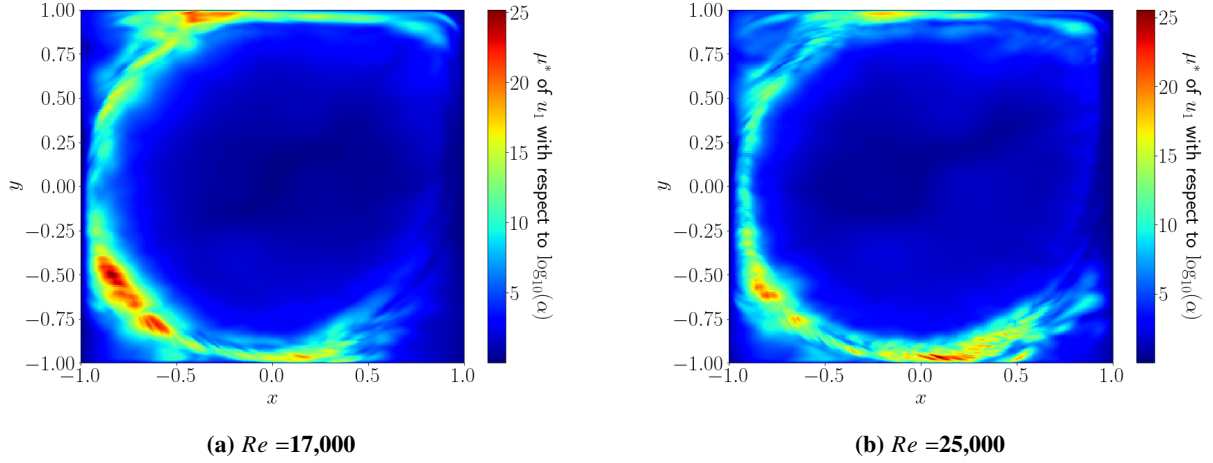


**Fig. 3** Morris mean absolute sensitivity of  $u^x$  to boundary condition at (a)  $Re = 17,000$  and (b)  $Re = 25,000$ .

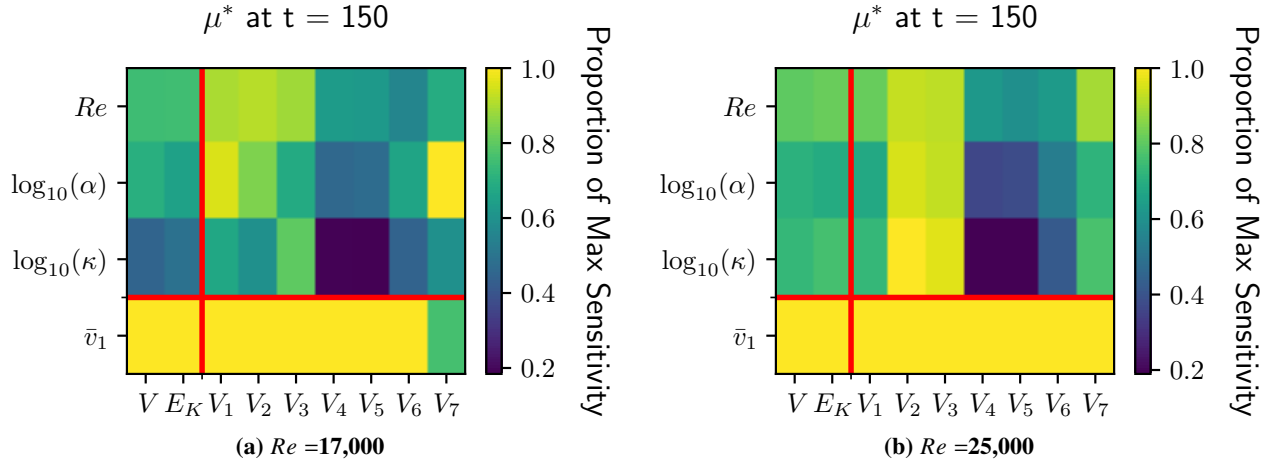


**Fig. 4** Morris mean absolute sensitivity results for global and local quantities at (a)  $Re = 17,000$  and (b)  $Re = 25,000$ . Each cell is  $\mu^*$  for the corresponding quantity (x-axis) and parameter (y-axis), divided by the maximum  $\mu^*$  for that quantity.

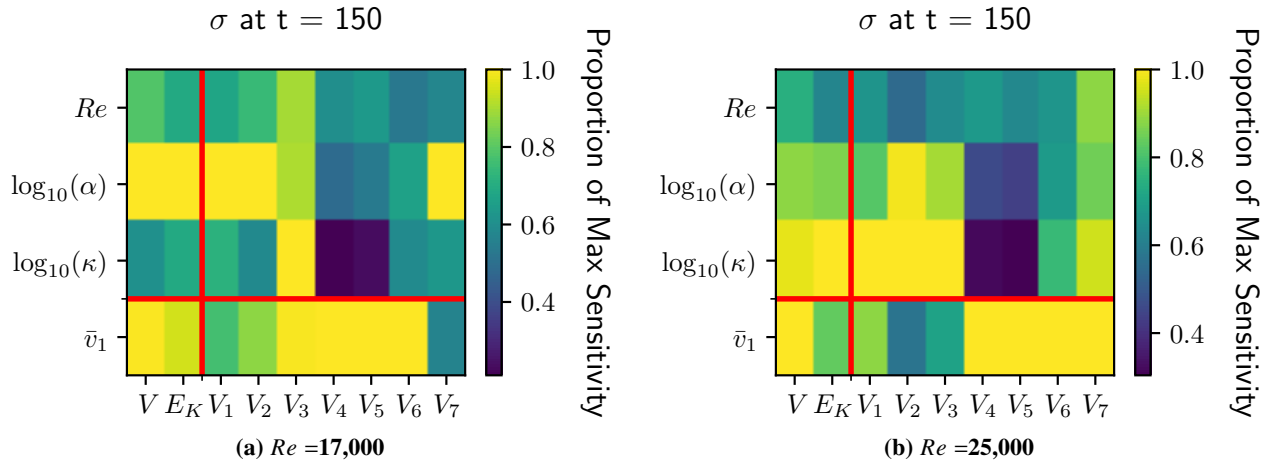


**Fig. 5** Morris standard deviation of sensitivity indices for global and local quantities at (a)  $Re = 17,000$  and (b)  $Re = 25,000$ . Each cell is  $\sigma^*$  for the corresponding quantity (x-axis) and parameter (y-axis), divided by the maximum  $\sigma^*$  for that quantity.

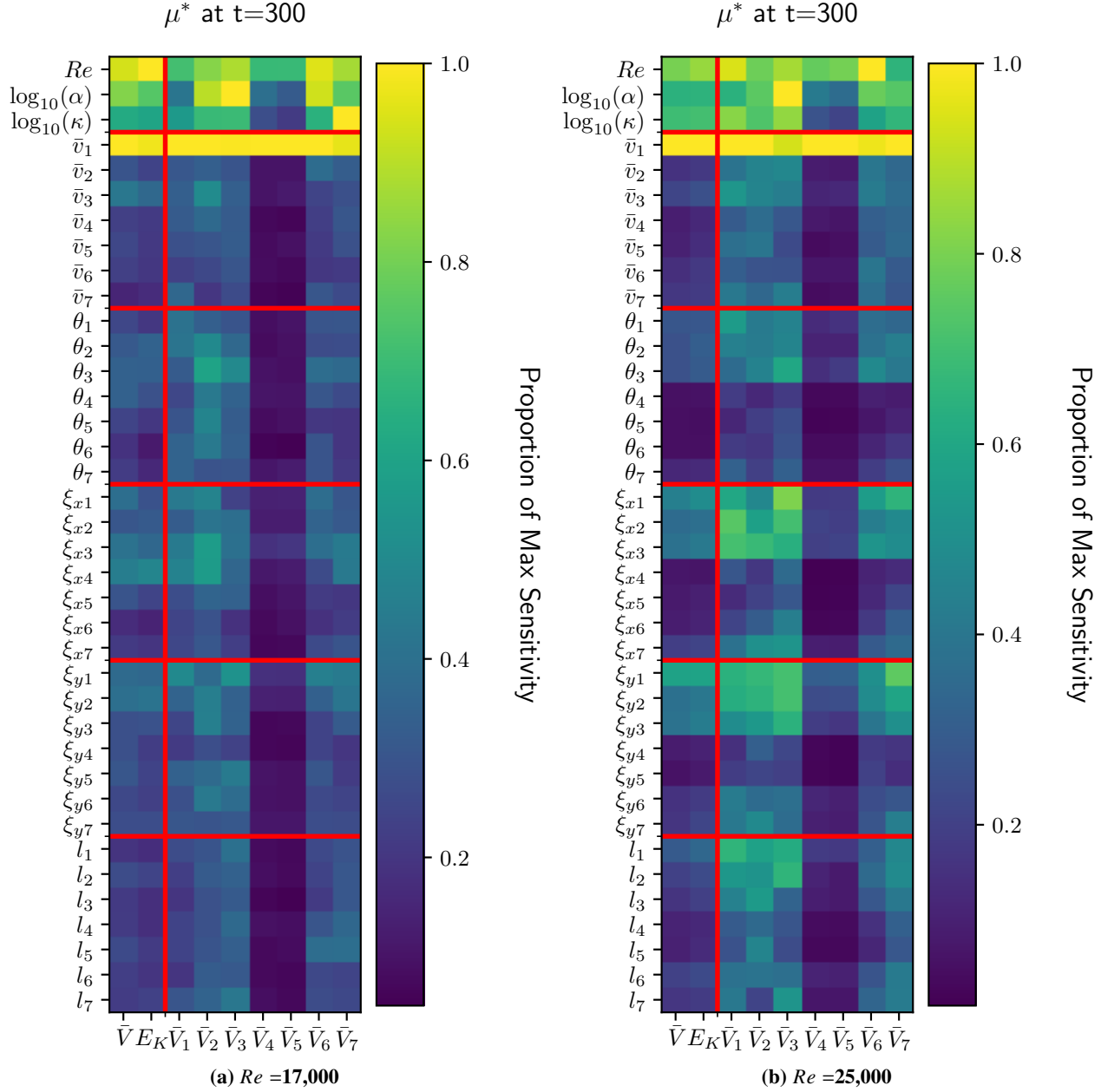


**Fig. 6** Morris mean absolute sensitivity results for global and local quantities at  $t = 300$  and (a)  $Re = 17,000$  and (b)  $Re = 25,000$ . Each cell is  $\mu^*$  for the corresponding quantity (x-axis) and parameter (y-axis), divided by the maximum  $\mu^*$  for that quantity.

## V. Conclusion

Quantification of CFD simulation variability with respect to boundary conditions and Reynolds number is a critical step to minimizing risk during planetary entry, descent and landing (EDL). However, high-fidelity direct numerical simulations are too computationally expensive for most sensitivity analysis while traditional proper orthogonal decomposition-based reduced order models (POD-ROMs) do not allow for adjustment of boundary conditions. We implement a novel solution to this limitation by using POD-ROMs with boundary penalties (BP-POD-ROM) to allow perturbation of boundary conditions, making sensitivity analysis feasible. We tested sensitivity of boundary conditions using a BP-POD-ROM on a lid-driven cavity test case at  $Re = 17,000$  and  $Re = 25,000$ , confirming a BP-POD-ROM constructed with regularized lid-driven cavity data exhibits high sensitivity to the boundary condition when perturbing towards a regularized boundary condition in the area of greatest anticipated change behind the driving lid and in the lower corner vorticity regions. This result is also congruent with comparisons of flow characteristics for regularized and unregularized lid-driven cavities, which have the greatest variation between boundary conditions and Reynolds numbers in these regions [13, 14].

We found kinetic energy and vorticity were rarely more sensitive to the boundary condition  $\alpha$  or penalty strength  $\kappa$  than Reynolds number or the velocity of the mean-reduction in the top-left,  $\bar{v}_1$ . We anticipate the BP-POD-ROM to be highly sensitive to the mean-reduction in the top-left since it influences the structure of POD modes at the boundary perturbations, thereby affecting the structure of modes that are strengthened and weakened by the penalty. Except for the velocity in the top-left, all quantities were insensitive to the mean-reduction at  $t = 150$ , confirming that perturbations to the mean-reduction in areas minimally affected by the boundary condition or Reynolds number do not produce vorticity. However, sensitivity to mean-reduction parameters did increase with longer time-integration, potentially introducing model error. Finally, sensitivity of each velocity cell rather than integrated quantities showed that the velocity was sensitive to the boundary condition in the expected high-vorticity areas, but not at the corners with boundary discontinuities.

The BP-POD-ROM provides a novel approach to sensitivity analysis of CFD data. By specifying boundary conditions in a Galerkin POD-ROM in this way, the approach allows sensitivity analysis of many physical parameters, such as surface roughness, that are too computationally intensive to study with high-fidelity simulations. For future research, we plan to extend the boundary penalty method to measure sensitivity of POD-ROMs in more complex models such as planetary EDL. We will formulate POD bases from high-fidelity FUN3D simulations of compressible flows around the Orion lander geometry [22]. Sensitivity analysis of the resulting Galerkin POD-ROMs will quantify the influence on key integrated quantities, such as kinetic energy and lift coefficients, of surface roughness of each lander panel along with nondimensional quantities such as Reynolds and Mach numbers. The resulting sensitivities can be used to focus future CFD simulations to decrease uncertainty in high sensitivity parameters.

## Appendix

### A. Parameter Values and Sampling Ranges

Table A.1 shows the list of model parameters, base values, and sampling ranges for sensitivity analysis. Note that base values are not used in computation of sensitivity indices and are either nominal values for the initial data or the assumed parameters for the mean-reduction displayed in Figure 1.

**Table A.1** Base parameter values and sampling ranges for Morris screening.

Parameter	Base Value	Sampling Ranges	Parameter	Base Value	Sampling Ranges
$Re$ (17,000 Case)	17,000	[11,000, 20,000]	$\bar{v}_1$	.95	[0.7125, 1.1875]
$Re$ (25,000 Case)	25,000	[19,000, 28,000]	$\bar{v}_2$	.5	[0.375, 0.625]
$\log_{10}(\alpha)$	0	[-2, 0]	$\bar{v}_3$	.5	[0.7125, 1.1875]
$\log_{10}(\kappa)$	-12	[-12, 0]	$\bar{v}_4$	.1	[0.075, 0.125]
$\xi_{x1}$	-0.75	[-0.9375, -0.5625]	$\bar{v}_5$	.1	[0.075, 0.125]
$\xi_{x2}$	-0.75	[-0.9375, -0.5625]	$\bar{v}_6$	.1	[0.075, 0.125]
$\xi_{x3}$	0.75	[0.5625, 0.9375]	$\bar{v}_7$	.1	[0.075, 0.125]
$\xi_{x4}$	-0.2	[-0.25, -0.15]	$\theta_1$	0	[0, $2\pi$ ]
$\xi_{x5}$	0.2	[0.15, -0.25]	$\theta_2$	$\frac{3\pi}{4}$	[0, $2\pi$ ]
$\xi_{x6}$	0.5	[0.375, 0.625]	$\theta_3$	$\frac{\pi}{4}$	[0, $2\pi$ ]
$\xi_{x7}$	0.75	[0.5625, 0.9375]	$\theta_4$	0	[0, $2\pi$ ]
$\xi_{y1}$	0.75	[0.5625, 0.9375, ]	$\theta_5$	0	[0, $2\pi$ ]
$\xi_{y2}$	-0.75	[-0.9375, -0.5625]	$\theta_6$	0	[0, $2\pi$ ]
$\xi_{y2}$	-0.75	[-0.9375, -0.5625]	$\theta_7$	0	[0, $2\pi$ ]
$\xi_{y4}$	-0.2	[-0.25, -0.15]	$l_1$	1	[.75, 1.25]
$\xi_{y5}$	0.2	[0.15, 0.25]	$l_2$	1.5	[1.125, 1.875]
$\xi_{y6}$	0.5	[0.375, 0.625]	$l_3$	1.5	[1.125, 1.875]
$\xi_{y7}$	0.75	[0.5625, 0.9375]	$l_4$	1	[.75, 1.25]
			$l_5$	1	[.75, 1.25]
			$l_6$	1	[.75, 1.25]
			$l_7$	1	[.75, 1.25]

## B. Additional Sensitivity Plots

Figures B.1 and B.2 are the full plots of the  $\mu^*$  and  $\sigma^*$  sensitivity indices. Figure B.3 shows the unscaled  $\mu^*$  sensitivity of locally integrated vorticities to all parameters. Figure B.4 shows the scaled  $\sigma^*$  sensitivity of all quantities to all parameters.

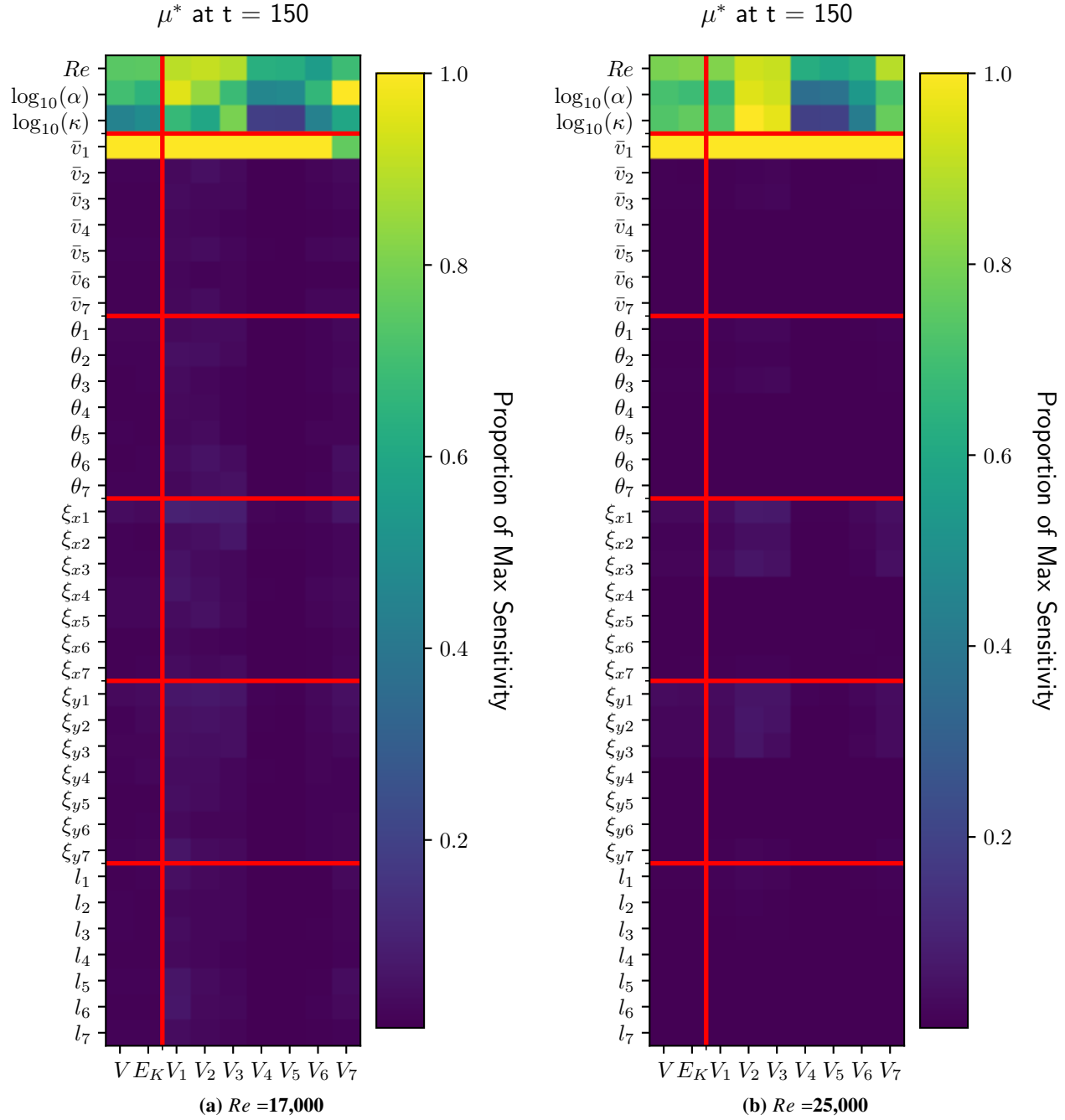


**Fig. B.1** Morris mean absolute sensitivity results for global and local quantities at  $Re = 17,000$  and  $Re = 25,000$ . Each cell is  $\mu^*$  for the corresponding quantity (x-axis) and parameter (y-axis), divided by the maximum  $\mu^*$  for that quantity.

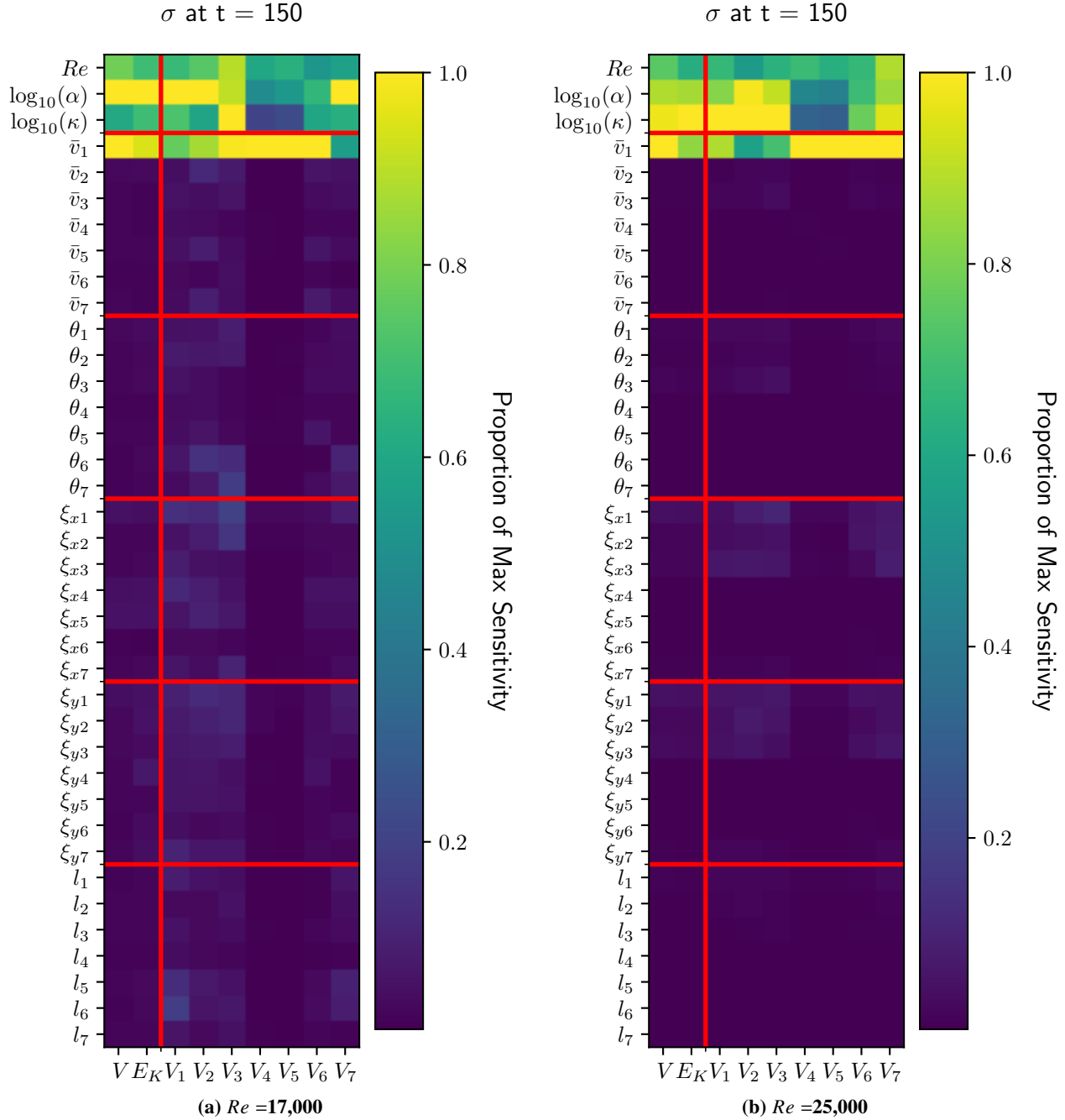


**Fig. B.2** Morris standard deviation of sensitivity indices for global and local quantities. Each cell is  $\sigma^*$  for the corresponding quantity (x-axis) and parameter (y-axis), divided by the maximum  $\sigma^*$  for that quantity.

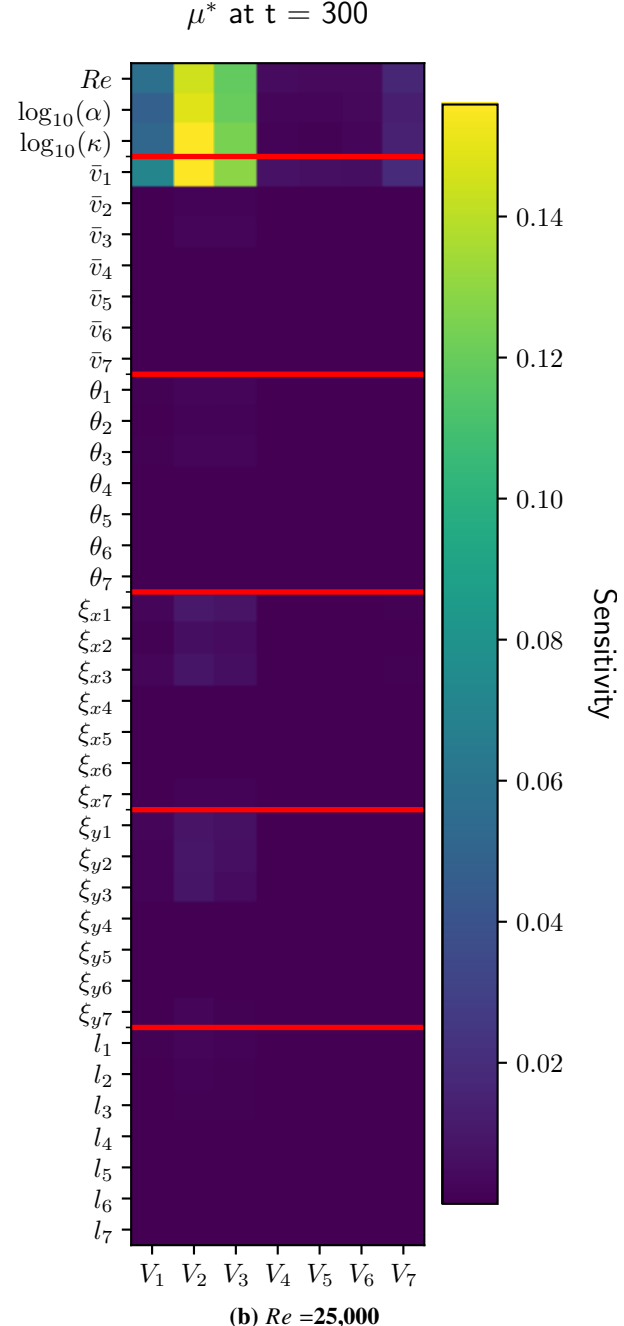
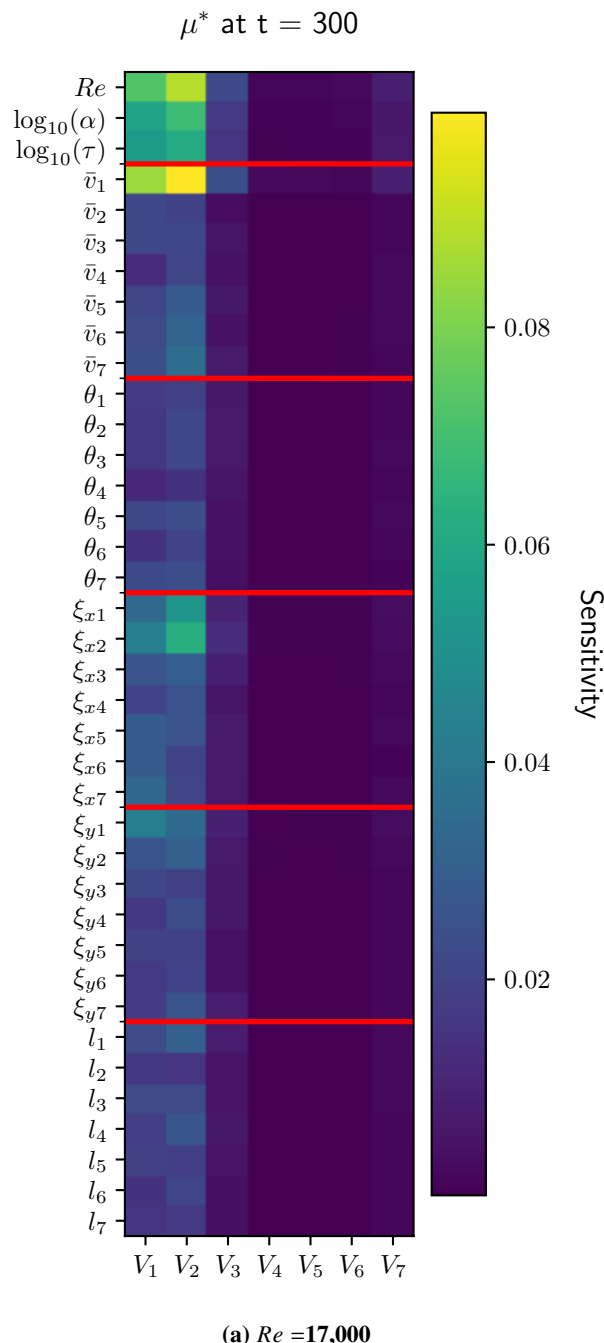


**Fig. B.3** Morris mean absolute sensitivity results for global and local quantities at  $t = 300$ . Each cell is  $\mu^*$  for the corresponding quantity (x-axis) and parameter (y-axis).

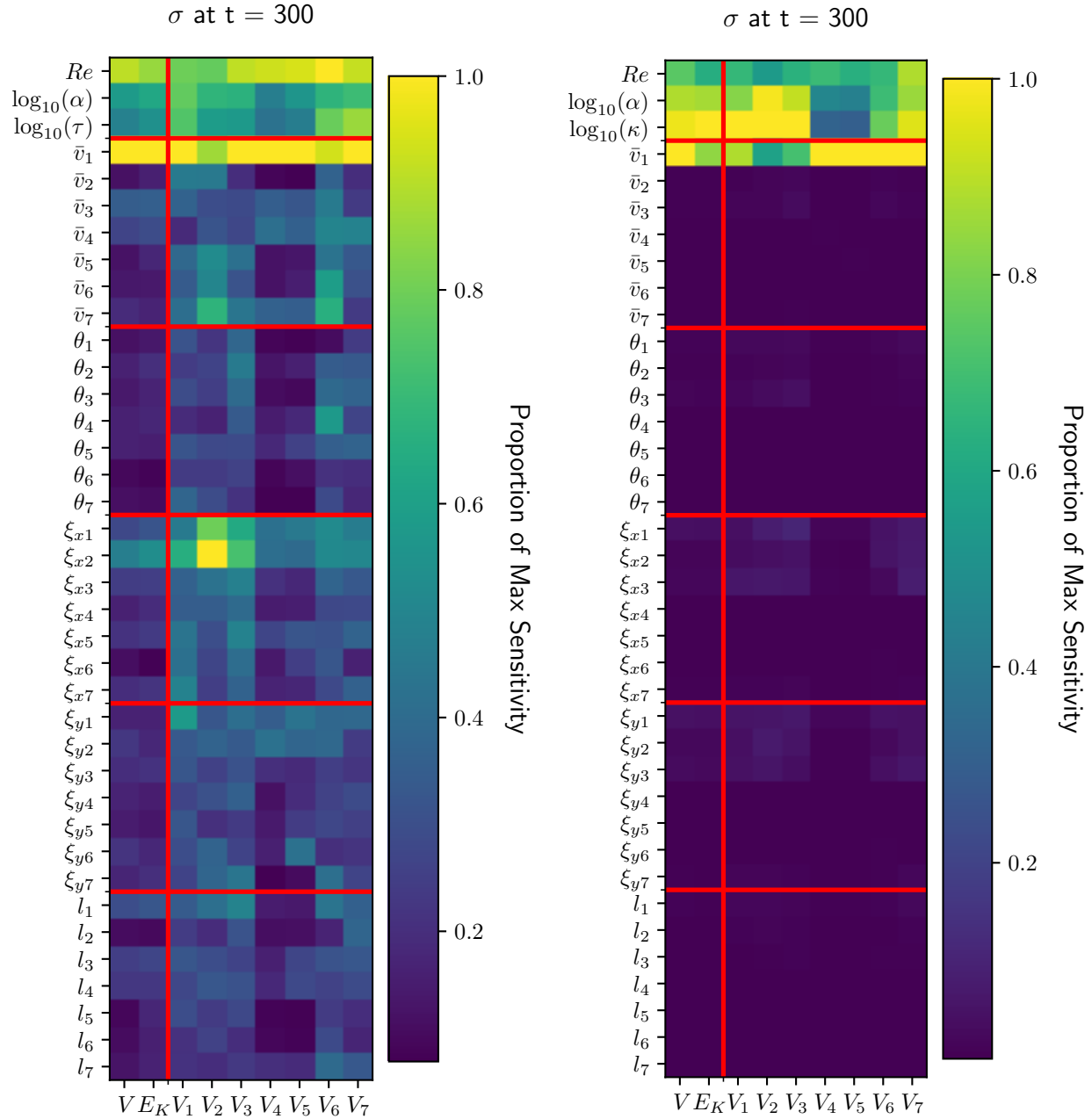


**Fig. B.4** Morris mean absolute sensitivity results for global and local quantities at  $t = 300$ . Each cell is  $\mu^*$  for the corresponding quantity (x-axis) and parameter (y-axis).

## Acknowledgments

This work was authored by employees of the University of Southern California and North Carolina State University under Contract No. 80LARC21CA002 and 80LARC21CA003 with the National Aeronautics and Space Administration. The United States Government retains and the publisher, by accepting the article for publication, acknowledges that the United States Government retains a nonexclusive, paid-up, irrevocable, worldwide license to reproduce, prepare derivative works, distribute copies to the public, and perform publicly and display publicly, or allow others to do so, for United States Government purposes. All other rights are reserved by the copyright owner.

## References

- [1] Snyder, S., Wignall, T., Green, J. S., Kumar, S. G., Lee, M. W., Nakamura-Zimmerer, T., Scoggins, J. B., and Williams, R. A., “AeroFusion: Data Fusion and Uncertainty Quantification for Lander Vehicles,” *AIAA Science and Technology Forum and Exposition*, 2023, pp. 0–12. <https://doi.org/10.2514/6.2023-1182>.
- [2] Van Belleghem, M., Steeman, H.-J., Steeman, M., Janssens, A., and De Paepe, M., “Sensitivity analysis of CFD coupled non-isothermal heat and moisture modelling,” *Building and Environment*, Vol. 45, No. 11, 2010, pp. 2485–2496. <https://doi.org/10.1016/j.buildenv.2010.05.011>.
- [3] Amato, D., Hume, S., Grace, M., Roelke, E., and Mcmahon, J., “Mars EDL and Aerocapture Guidance under Dynamic Uncertainty,” *AAS/AIAA Astrodynamics Specialist Conference*, 2020, pp. 1–18.
- [4] Lorenzoni, L. V., SanMartin, M., Steltzner, A., and Chen, A., “Preliminary Assessment of MSL EDL Sensitivity to Martian Environments,” *2007 IEEE Aerospace Conference*, 2007, pp. 1–8. <https://doi.org/10.1109/AERO.2007.352822>.
- [5] Smith, R. C., *Uncertainty Quantification: Theory, Implementation, and Applications*, Society for Industrial and Applied Mathematics, Philadelphia, PA, 2014.
- [6] Morris, M. D., “Factorial Sampling Plans for Preliminary Computational Experiments,” *Technometrics*, Vol. 33, No. 2, 1991, pp. 161–174. <https://doi.org/10.1080/00401706.1991.10484804>.
- [7] Saltelli, A., Tarantola, S., Campolongo, F., and Ratto, M., *Sensitivity Analysis in Practice: A Guide to Assessing Scientific Models*, John Wiley & Sons Ltd, West Sussex, England, 2004.
- [8] Sirisup, S., and Karniadakis, G., “Stability and accuracy of periodic flow solutions obtained by a POD-penalty method,” *Physica D: Nonlinear Phenomena*, Vol. 202, 2005, pp. 218–237. <https://doi.org/10.1016/j.physd.2005.02.006>.
- [9] Bizon, K., and Continillo, G., “Reduced order modelling of chemical reactors with recycle by means of POD-penalty method,” *Computers & Chemical Engineering*, Vol. 39, 2012, pp. 22–32. <https://doi.org/10.1016/j.compchemeng.2011.10.001>.
- [10] Mastroddi, F., Stella, F., Cantiani, D., and Vetrano, F., “Linearized aeroelastic gust response analysis of a launch vehicle,” *Journal of Spacecraft and Rockets*, Vol. 48, No. 3, 2011, pp. 420–432. <https://doi.org/10.2514/1.47268>.
- [11] Krogstadt, P., and Antonia, R., “Surface roughness effects in turbulent boundary layers,” *Experiments in Fluids*, Vol. 27, No. 5, 1999, pp. 450–460. <https://doi.org/10.1007/s003480050370>.
- [12] Sousa, R., Poole, R., Afonso, A., Pinho, F., Oliveira, P., Morozov, A., and Alves, M., “Lid-driven cavity flow of viscoelastic liquids,” *Journal of Non-Newtonian Fluid Mechanics*, Vol. 234, 2016, pp. 129–138. <https://doi.org/10.1016/j.jnnfm.2016.03.001>.
- [13] Lee, M. W., Dowell, E. H., and Balajewicz, M. J., “A study of the regularized lid-driven cavity’s progression to chaos,” *Communications in Nonlinear Science and Numerical Simulation*, Vol. 71, 2019, pp. 50–72. <https://doi.org/10.1016/j.cnsns.2018.11.010>.
- [14] Nuriev, A. N., Egorov, A. G., and Zaitseva, O. N., “Bifurcation analysis of steady-state flows in the lid-driven cavity,” *Fluid Dynamics Research*, Vol. 48, No. 6, 2016. <https://doi.org/10.1088/0169-5983/48/6/061405>.
- [15] Kucherenko, S., Rodriguez-Fernandez, M., Pantelides, C., and Shah, N., “Monte Carlo evaluation of derivative-based global sensitivity measures,” *Reliability Engineering ,& System Safety*, Vol. 94, No. 7, 2009, pp. 1135–1148. <https://doi.org/10.1016/j.ress.2008.05.006>.
- [16] Campolongo, F., Cariboni, J., and Saltelli, A., “An effective screening design for sensitivity analysis of large models,” *Environmental Modelling & Software*, Vol. 22, No. 10, 2007, pp. 1509–1518. <https://doi.org/10.1016/j.envsoft.2006.10.004>.

- [17] Lorenzi, S., Cammi, A., Luzzi, L., and Rozza, G., “POD-Galerkin method for finite volume approximation of Navier–Stokes and RANS equations,” *Computer Methods in Applied Mechanics and Engineering*, Vol. 311, 2016, pp. 151–179. <https://doi.org/10.1016/j.cma.2016.08.006>.
- [18] Lee, M. W., “On Improving the Predictable Accuracy of Reduced-order Models for Fluid Flows,” Ph.D. thesis, Duke University, 2020.
- [19] Shankar, P., and Deshpande, M., “Fluid mechanics in the driven cavity,” *Annual review of fluid mechanics*, Vol. 32, No. 1, 2000, pp. 93–136. <https://doi.org/10.1146/annurev.fluid.32.1.93>.
- [20] Shen, J., “Hopf bifurcation of the unsteady regularized driven cavity flow,” *Journal of Computational Physics*, Vol. 95, No. 1, 1991, pp. 228–245. [https://doi.org/10.1016/0021-9991\(91\)90261-I](https://doi.org/10.1016/0021-9991(91)90261-I).
- [21] Lee, M. W., “Steady State 2D Regularized Lid-Driven Cavity High-resolution Spatiotemporal Snapshots,” *Mendeley Data*, Vol. 1, 2021. <https://doi.org/10.17632/mbx34thp2y.1>.
- [22] Biedron, R. T., Carlson, J.-R., Derlaga, J. M., Gnoffo, P. A., Hammond, D. P., Jacobson, K. E., Jones, W. T., Kleb, B., Lee-Rausch, E. M., Nielsen, E. J., Park, M. A., Rumsey, C. L., Thomas, J. L., Thompson, K. B., Walden, A. C., Wang, L., and Wood, W. A., “FUN3D Manual: 13.7,” Tech. Rep. No. NASA/TM-20205010139, National Aeronautics and Space Administration (NASA), Langley Research Center, Hampton, Virginia (United States), 2021.